# Charge Transport in a Multiterminal DNA Tetrahedron: Interplay among Contact Position, Disorder, and Base-Pair Mismatch

Pei-Jia Hu,[1] Si-Xian Wang,[1] Xiao-Feng Chen,[1,2] Xiao-Hui Gao,[1] Tie-Feng Fang,[3] Ai-Min Guo,[1,*] and Qing-Feng Sun[4,5,6]

[1] *Hunan Key Laboratory for Super-microstructure and Ultrafast Process, School of Physics and Electronics, Central South University, Changsha 410083, China*

[2] *School of Physical Science and Technology, Lanzhou University, Lanzhou 730000, China*

[3] *School of Sciences, Nantong University, Nantong 226019, China*

[4] *International Center for Quantum Materials, School of Physics, Peking University, Beijing 100871, China*

[5] *Collaborative Innovation Center of Quantum Matter, Beijing 100871, China*

[6] *CAS Center for Excellence in Topological Quantum Computation, University of Chinese Academy of Sciences, Beijing 100190, China*

(Received 21 July 2021; revised 23 October 2021; accepted 9 February 2022; published 28 February 2022)

As a secondary structure of DNA, DNA tetrahedra exhibit intriguing charge-transport phenomena and provide a promising platform for wide applications like biosensors, as shown in recent electrochemical experiments. Here, we study charge transport in a multiterminal DNA tetrahedron, finding that its charge-transport properties strongly depend upon the interplay of contact position, on-site energy disorder, and base-pair mismatch. Our results indicate that this multiterminal DNA tetrahedron behaves as a nanoscale charge splitter when the source is contacted at the top vertex. Besides, we find that the charge-transport efficiency is nearly independent of the contact position in the weak disorder regime, and is dramatically declined by the occurrence of a single base-pair mismatch between the source and the drain, in accordance with experimental results [J. Am. Chem. Soc. **134**, 13148 (2012); Chem. Sci. **9**, 979 (2018)]. By contrast, the charge-transport efficiency will be enhanced monotonically by shifting the source toward the drain in the strong disorder regime, and be increased when the base-pair mismatch takes place exactly at the contact position. In particular, when the source moves successively from the top vertex to the drain, the charge transport through the tetrahedral DNA device can be separated into three regimes, ranging from disorder-induced linear decrement of conductance to disorder-insensitive charge transport, and to disorder-enhanced charge transport. Finally, we predict that the DNA tetrahedron functions as a more efficient spin filter compared to double-stranded DNA and as a nanoscale spin splitter with opposite spin polarization observed at different drains. These results could be readily checked by electrochemical measurements and help for designing intriguing DNA tetrahedron-based molecular nanodevices.

DOI: 10.1103/PhysRevApplied.17.024074

## I. INTRODUCTION

Since the original proposal by Eley and Spivey that $\pi$ stacking along the helix axis could provide a natural pathway for conducting electrons in DNA molecules [1], their charge-transport properties have been attracting extensive attention among the physics, chemistry, and biology communities [2–5], finding that DNA functions as a promising candidate for molecular electronics. Recent charge-transport experiments have demonstrated a number of fascinating phenomena in double-stranded DNA (dsDNA) by means of advanced experimental techniques [6–12]. For example, Guo *et al.* have proposed a DNA-based molecular rectifier with high rectification ratio upon intercalation of coralyne into a single dsDNA [9]. Göhler *et al.* have reported that spin-unpolarized electrons become highly spin polarized when transmitting through a self-assembled monolayer of dsDNA [6], which is termed as chirality-induced spin selectivity (CISS) [13]. This CISS effect has been confirmed in a variety of chiral molecules by numerous experimental and theoretical groups (see Refs. [14–16] for a review), and opens promising avenues for wide applications based on chiral molecules, like magnetic memory devices without permanent magnets [17] and separation of two enantiomers [18]. Beyond current experimental observations, many interesting phenomena have also been predicted in dsDNA devices [19–27], such as the emergence of Majorana zero modes and topological charge

*aimin.guo@csu.edu.cn

 

pumping. However, when the $\pi$ stacking is perturbed by either base-pair mismatch or oxidative damage, the charge transport through DNA could be significantly decreased, as demonstrated by experimental and theoretical works [28–36].

Besides the traditional double helix, DNA can form diverse two- and three-dimensional (3D) nanostructures like DNA tetrahedra [37–43]. The DNA tetrahedron consists of six Watson-Crick-paired edges linked by unpaired hinge nucleobases, as illustrated in Fig. 1. Here, each double-stranded edge is named as the combination of two different lines, including the RO, RM, RB, OM, OB, and MB edges. This DNA nanostructure possesses several superior advantages. (i) The DNA tetrahedron can be self-assembled from four well-designed single-stranded DNA (ssDNA) (see the red, orange, magenta, and black lines in Fig. 1), which could be accomplished in only a few seconds and be much simpler compared to the synthesis of other DNA derivatives, as reported by Turberfield *et al.* [39,40]. (ii) The DNA tetrahedron has high mechanical rigidity and could stay normal to the surface, thus avoiding the crowding effect and sample collision, which occur in dense dsDNA monolayers [44,45]. (iii) The DNA tetrahedron is capable of entering cells efficiently and can thus deliver cargoes, such as drugs, across cells using its hollow structure [46–49].

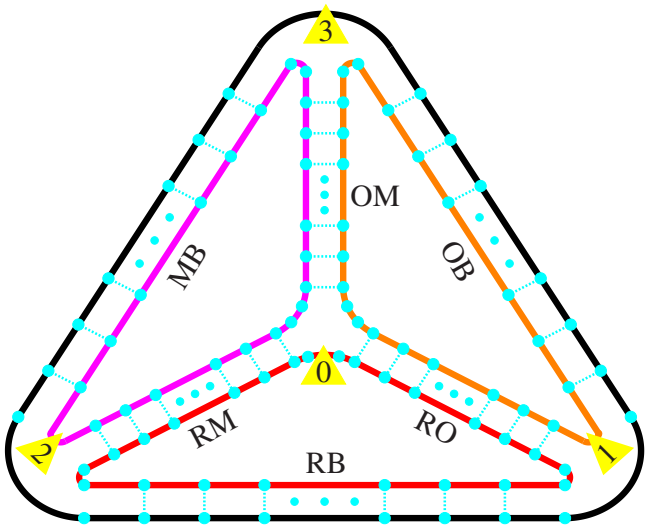


FIG. 1. Top view of a DNA tetrahedron composed of six Watson-Crick-paired edges, where two neighboring edges are linked by unpaired hinge nucleobases. This DNA tetrahedron can be self-assembled from four specifically designed single-stranded DNA, which are represented by the red, orange, magenta, and black lines. Each double-stranded edge can then be labeled by combining two different lines, including the RO, RM, RB, OM, OB, and MB edges. This three-dimensional DNA structure is contacted by four nonmagnetic electrodes $e_0$, $e_1$, $e_2$, and $e_3$ (see the yellow triangles indicated by arabic numerals 0, 1, 2, and 3). The electrode $e_0$ can move along the RO edge and act as the source, and the other electrodes are fixed at the three bottom vertices $D_{j\,(j=1,2,3)}$ and serve as the drain, just as electrochemical experiments [51,53]. Here, $e_0$ is contacted at the top vertex $D_0$ of the DNA tetrahedron with $P = 0$ (see text), the big cyan spheres denote nucleobases, and the dotted lines stand for hydrogen bonding within a single base pair. For clarity, the helical structure is not presented.

Specifically, Fan *et al.* have designed a four-terminal tetrahedral DNA device [50–52], where the top vertex $D_0$ is connected to a redox molecule (electrode $e_0$) and the three bottom ones $D_{j\,(j=1,2,3)}$ are chemisorbed on a surface via thiol groups to immobilize the DNA tetrahedron, as shown in Fig. 1. By performing electrochemical experiments, the charge transmission through this multiterminal DNA tetrahedron has been intensively studied and presents several distinct characteristics [50–53]. (i) When the redox molecule of methylene blue is separated from the surface by either four or thirteen nucleobases, the charge-transport efficiency keeps almost the same, implying that the charge transport along the DNA tetrahedron may be insensitive to the position of the redox molecule. (ii) When a single base-pair mismatch takes place between the redox molecule and the surface, the charge-transport efficiency could diminish dramatically. In addition, many experiments have demonstrated that the DNA tetrahedron provides a promising platform for realizing biosensors which are superior to dsDNA [50–59], where the charge transport plays a vital role. However, the underlying physics remains unclear regarding charge transport through this multiterminal DNA tetrahedron.

In this paper, we study theoretically the charge transport through a multiterminal DNA tetrahedron as in electrochemical experiments by considering contact position, on-site energy disorder, and base-pair mismatch. Here, the variation of the contact position is achieved by moving the source $e_0$ along the RO edge, and the three drains $e_1$, $e_2$, and $e_3$ are fixed at the bottom vertices $D_1$, $D_2$, and $D_3$, respectively, as shown by the yellow triangles in Fig. 1. Our results indicate that the charge-transport properties of the DNA tetrahedron strongly depend on the interplay among the contact position, the on-site energy disorder, and the base-pair mismatch, because of the multiple transport pathways. When $e_0$ is contacted at the top vertex $D_0$, this multiterminal DNA tetrahedron behaves as a nanoscale charge splitter, where similar transmission spectra and considerable conductance are observed at the three drains. We then focus on the charge transport detected at the specific drain $e_1$, finding that the charge transport through the DNA tetrahedron presents several intriguing phenomena when $e_0$ moves along the RO edge. First, the charge-transport efficiency is approximately independent of the source position in the weak disorder regime when $e_0$ is separated from $e_1$ by at least a few nucleobases, and could be dramatically reduced by the occurrence of a single base-pair mismatch between

$e_0$ and $e_1$, both of which are consistent with experimental results [51,53]. Second, the charge-transport efficiency could be enhanced monotonically by shifting $e_0$ toward $e_1$ in the strong disorder regime, and be increased when the base-pair mismatch takes place exactly at the source position. Third, when $e_0$ moves successively from $D_0$ to $e_1$, the charge transport through the DNA tetrahedron can be divided into three regimes, ranging from disorder-induced linear decrement of conductance to disorder-insensitive charge transport, and to disorder-enhanced charge transport, which is contrary to the common viewpoint that the charge-transmission ability should become poorer in the stronger disorder regime. Finally, we predict that the DNA tetrahedron could exhibit significant spin-filtering effect, with spin-filtration efficiency much larger than dsDNA molecules. In particular, the DNA tetrahedron functions as a nanoscale spin splitter with opposite spin-polarized direction observed at the two drains $e_1$ and $e_2$, which may be applied to separate spin-unpolarized electrons into spin-up electrons and spin-down ones. The underlying physics of all these transport phenomena is analyzed. These results could help for improving performance of biosensors and for designing intriguing electronic (spintronics) devices on the basis of the DNA tetrahedron by taking into account the charge and/or spin degrees of freedom.

The rest of the paper is constructed as follows. Section II presents the model Hamiltonian of a multiterminal DNA tetrahedron and Green's function. Section III shows the numerical results and discussion. Section III A studies the influence of the contact position and the on-site energy disorder on the charge transport along the DNA tetrahedron, Sec. III B considers the base-pair mismatch effect, and Sec. III C investigates the spin-filtering effect. Finally, the results are concluded in Sec. IV.

## II. MODEL AND METHOD

The charge transport through a multiterminal DNA tetrahedron can be described by the model Hamiltonian $\mathcal{H} = \mathcal{H}_m + \mathcal{H}_d + \mathcal{H}_e$. The first term, $\mathcal{H}_m$, is the Hamiltonian of an isolated DNA tetrahedron including both double-stranded edges and unpaired hinge nucleobases, which reads [60]

$$\mathcal{H}_m = \sum_{j=0}^{3}\left\{\sum_{n=1}^{N_j}[\varepsilon_{jn}c_{jn}^{\dagger}c_{jn} + t_{n,n+1}^{(j)}c_{jn}^{\dagger}c_{jn+1}] + \sum_{s=1}^{3}\sum_{n=j_s}^{j_s+N-2} it_{\mathrm{SO}}c_{jn}^{\dagger}[\sigma_n^{(\eta)} + \sigma_{n+1}^{(\eta)}]c_{jn+1} + \mathrm{H.c.}\right\} + \sum_{\langle jn,j'n'\rangle}\lambda c_{jn}^{\dagger}c_{j'n'}. \quad (1)$$

Here, $c_{jn}^{\dagger} = (c_{jn\uparrow}^{\dagger}, c_{jn\downarrow}^{\dagger})$ is the creation operator of an electron at site $\{j,n\}$, with $c_{jN_j+1}^{\dagger} = c_{j1}^{\dagger}$, $j$ labeling the ssDNA whose length is $N_j$ (see the red, orange, magenta, and black lines in Fig. 1) and $n$ the nucleobase index (see the big cyan spheres in Fig. 1). $\varepsilon_{jn}$ is the on-site energy, $t_{n,n+1}^{(j)}$ ($\lambda$) is the intrastrand (interstrand) coupling, and $t_{\mathrm{SO}}$ the spin-orbit coupling (SOC) parameter. Each ssDNA contains three segments $s = 1$, 2, and 3, all of which pair with the complementary ssDNA segment and lead to six self-assembled double-stranded edges (Fig. 1). $j_s$ is the nucleobase index at which the base pairing begins in the $s$th segment of the $j$th ssDNA and $N$ is the length of the double-stranded edges. The SOC term is expressed as $\sigma_n^{(\eta)} = \sigma_z\cos\theta - (-1)^{\eta}\{\sigma_x\sin[(n-j_s)\Delta\varphi] - \sigma_y\cos[(n-j_s)\Delta\varphi]\}\sin\theta$ [60], where $\sigma_{x,y,z}$ are the Pauli matrices, $\theta$ is the space angle between the helical strand and the plane perpendicular to the corresponding helix axis, $\Delta\varphi$ is the twist angle between two neighboring base pairs, and $\eta = 1,2$ is the strand index of double-stranded edges. $\langle\cdots\rangle$ represents the nearest-neighbor nucleobases between two complementary segments of the $j$th and $j'$th ssDNA.

The second term, $\mathcal{H}_d$, describes the dephasing processes during the charge transport in the DNA tetrahedron, which are caused by inelastic scatterings, such as the electron-phonon interaction and the electron-electron interaction. These dephasing processes can be simulated by connecting each nucleobase to a Büttiker virtual electrode [60].

The last term, $\mathcal{H}_e$, represents the four nonmagnetic electrodes and their couplings to the DNA tetrahedron (see the yellow triangles in Fig. 1). The drain electrodes $e_1$, $e_2$, and $e_3$, aiming to anchoring the DNA tetrahedron on the substrate, are contacted at the three bottom vertices $D_1$, $D_2$, and $D_3$, respectively. Their Hamiltonian is expressed as

$$\mathcal{H}_e^{(j)} = \sum_k[\varepsilon_{jk}a_{jk}^{\dagger}a_{jk} + \tau a_{jk}^{\dagger}(c_{j1} + c_{jN_j}) + \mathrm{H.c.}]. \quad (2)$$

Here, $a_{jk}^{\dagger} = (a_{jk\uparrow}^{\dagger}, a_{jk\downarrow}^{\dagger})$ is the creation operator of mode $k$ in the drain electrode $e_j$, and $\tau$ is the coupling between the DNA tetrahedron and the electrodes, with $j = 1$, 2, and 3. Notice that each electrode $e_{j\,(j=1,2,3)}$ is connected to both ends of the $j$th ssDNA. For the source electrode $e_0$, it can move along the RO edge and the Hamiltonian is

$$\mathcal{H}_e^{(0)} = \sum_k[\varepsilon_{0k}a_{0k}^{\dagger}a_{0k} + \tau a_{0k}^{\dagger}(c_{0P} + c_{0P+1}) + \mathrm{H.c.}], \quad (3)$$

where $e_0$ is connected to the $P$th and $P+1$th nucleobases of the 0th ssDNA, with $P$ being the contact position and $c_{00}^{\dagger} \equiv c_{0N_0}^{\dagger}$. Figure 1 presents a tetrahedral DNA device where $e_0$ is contacted at $D_0$ with $P = 0$. We emphasize that when an electrode is intercalated between two neighboring

nucleoases, the direct connection between these two nucleobases is replaced by indirect connection via this electrode and the corresponding intrastrand coupling disappears.

In the linear response regime with a small bias voltage between the source and the drain, the current flowing through the $p$th electrode (real or virtual) can be obtained from the Landauer-Büttiker formula and the nonequilibrium Green's function, which reads [61]

$$I_p = \frac{2e^2}{h} \sum_q T_{p,q} \left(V_q - V_p\right). \tag{4}$$

Here, $V_q$ and $V_p$ are, respectively, the voltages applied in the $q$th and $p$th electrodes, and

$$T_{p,q} = \mathrm{Tr}[\mathbf{\Gamma}_p \mathbf{G}^r \mathbf{\Gamma}_q \mathbf{G}^a] \tag{5}$$

is the transmission coefficient from the $q$th electrode to the $p$th one. Green's function $\mathbf{G}^r(E) = [\mathbf{G}^a(E)]^\dagger = [E\mathbf{I} - \mathbf{H}_m - \sum_p \mathbf{\Sigma}_p^r]^{-1}$ and the linewidth function $\mathbf{\Gamma}_p = i[\mathbf{\Sigma}_p^r - (\mathbf{\Sigma}_p^r)^\dagger]$, with $E$ the electron energy, $\mathbf{H}_m$ the Hamiltonian of the isolated DNA tetrahedron in the site representation, and $\mathbf{\Sigma}_p^r$ the retarded self-energy owing to the coupling to the $p$th electrode. In the wide-band limit, the retarded self-energy for the real electrodes is taken as $\Sigma_p^r = -i\pi\rho\tau^2 = -i\Gamma/2$ [60,61], with $\rho$ being the density of states of the real electrodes, and $\Gamma$ the coupling strength between the DNA tetrahedron and the real electrodes. Similarly, the retarded self-energy for the virtual electrodes is set to $\Sigma_p^r = -i\Gamma_d/2$, with $\Gamma_d$ the dephasing parameter. Here, the small bias voltage between the source and the drain is set to $V_{e_0} = V_b$ for $e_0$ and $V_{e_j} = 0$ for $e_{j\,(j=1,2,3)}$, and the net current flowing through each virtual electrode is zero. Under these boundary conditions, the voltages of the virtual electrodes can be calculated from Eq. (4). Then, the conductance of all the drains $e_{j\,(j=1,2,3)}$ can be obtained as

$$G_j = \frac{2e^2}{h} \sum_q T_{e_j,q} \frac{V_q}{V_b}. \tag{6}$$

## III. RESULTS AND DISCUSSION

We consider the case that all the double-stranded edges are identical homogeneous dsDNA molecules, e.g., poly(G)-poly(C), with G the guanine and C the cytosine. The on-site energy and the intrastrand coupling are set to $\varepsilon_{jn} = \varepsilon_{\mathrm{G}}$ and $t_{n,n+1}^{(j)} = t_{\mathrm{GG}}$ for the first strand, $\varepsilon_{jn} = \varepsilon_{\mathrm{C}}$ and $t_{n,n+1}^{(j)} = t_{\mathrm{CC}}$ for the second strand, and $\varepsilon_{jn} = \varepsilon_{\mathrm{G}}$ for the unpaired hinge nucleobases. As the paired nucleobase could be different from the unpaired one in the same ssDNA, the intrastrand coupling between two neighboring G and C nucleobases is taken as $t_{n,n+1}^{(j)} = t_{\mathrm{GC}}$. These model parameters are set to $\varepsilon_{\mathrm{G}} = 0$ (energy reference point), $\varepsilon_{\mathrm{C}} = 0.34$, $t_{\mathrm{GG}} = 0.08$, $t_{\mathrm{CC}} = t_{\mathrm{GC}} = -0.12$, and $\lambda = -0.17$, with the unit in eV, which locate within the range reported in previous works [62–66] and could allow for comparison between the charge- and spin-transport properties of the DNA tetrahedron and normal dsDNA molecules [60]. We point out that the significant features discussed below, such as the separation of two electronic bands by an energy gap, considerable conductances observed at different drains, and the splitting of transmission peaks, remain for different model parameters. The SOC strength is set to $t_{\mathrm{SO}} = 0.01$, and the structural parameters to $\theta \approx 0.66$ and $\Delta\phi = \pi/5$ [60]. The size of the DNA tetrahedron is set to $N = 17$, $N_0 = 57$, and $N_1 = N_2 = N_3 = 55$, just the same as the experiment [51]. The coupling parameter is $\Gamma = 1$ for the real electrodes, and the dephasing strength is $\Gamma_d = 10^{-4}$ for the virtual ones because the DNA tetrahedron presents higher mechanical rigidity compared to normal dsDNA molecules. Since the hinge nucleobases around the four vertices $D_{j\,(j=0,1,2,3)}$ are unpaired and cannot form a well-defined secondary structure, the corresponding intrastrand coupling is estimated to half of its initial value and the SOC is neglected. As a result, the SOC and the interstrand coupling exist only in the double-stranded edges.

### A. Contact position and disorder effects on charge transport along tetrahedral DNA devices

We first study the charge-transport properties of the tetrahedral DNA device in the absence of the on-site energy disorder when the source electrode is contacted at the top vertex $D_0$ with $P = 0$ (Fig. 1). Figure 2 shows the corresponding conductances $G_1$, $G_2$, and $G_3$ of the three drain electrodes, as a function of the electron energy $E$.

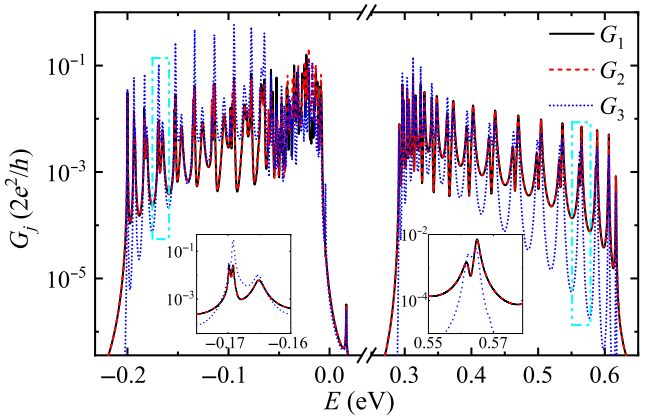


FIG. 2. Charge transport along the tetrahedral DNA device in the absence of the on-site energy disorder when the source electrode $e_0$ is contacted at the top vertex with $P = 0$. Energy-dependent conductance $G_1$ detected at the drain electrode $e_1$ (black-solid line), $G_2$ at $e_2$ (red-dashed line), and $G_3$ at $e_3$ (blue-dotted line). The left (right) inset shows the magnified view of $G_j$-$E$ in the left (right) cyan rectangle.

It clearly appears that the transmission spectra are quite similar at different drain electrodes and the corresponding conductances are considerable, because all the real electrodes are connected to the four nearly equivalent vertices $D_{j\,(j=0,1,2,3)}$ of the DNA tetrahedron when $P = 0$. This indicates that the multiterminal DNA tetrahedron could serve as a nanoscale charge splitter. By inspecting Fig. 2, one can see that all the transmission spectra consist of two electronic bands separated by an energy gap and thus the DNA tetrahedron exhibits semiconducting behavior when the Fermi energy situates in this gap. Besides, a number of pronounced transmission peaks and valleys can be found in each band and the density of peaks and valleys becomes larger when $E$ is close to the energy gap, owing to the SOC effect. These features are similar to a single dsDNA molecule [60,67], because the DNA tetrahedron consists of six identical dsDNA molecules.

It is interesting that for both bands of the DNA tetrahedron, each original transmission peak is usually split into a pair of minor peaks separated by a dip (see the insets of the magnified view of the two cyan rectangles in Fig. 2) and consequently there are $2(N-1)$ transmission peaks in the right band. This phenomenon is completely different from a single dsDNA [60,67] and can be understood from the multiple transport pathways between the source and the drain. Let us take electron flowing from $e_0$ to $e_1$ as an example. In this case, the electrons can transport via the multiple pathways, including

$$\begin{aligned} &D_0 \rightarrow \mathrm{RO} \rightarrow D_1, \\ &D_0 \rightarrow \mathrm{RM} \rightarrow D_2 \rightarrow \mathrm{RB} \rightarrow D_1, \\ &D_0 \rightarrow \mathrm{OM} \rightarrow D_3 \rightarrow \mathrm{OB} \rightarrow D_1, \\ &D_0 \rightarrow \mathrm{RM} \rightarrow D_2 \rightarrow \mathrm{MB} \rightarrow D_3 \rightarrow \mathrm{OB} \rightarrow D_1, \end{aligned} \tag{7}$$

and

$$D_0 \rightarrow \mathrm{OM} \rightarrow D_3 \rightarrow \mathrm{MB} \rightarrow D_2 \rightarrow \mathrm{RB} \rightarrow D_1.$$

One can infer from Eq. (7) that the second pathway is equivalent to the third one, because these two pathways contain the same number of the unpaired nucleobases and all the double-stranded edges are identical. In the strong scattering regime where $E$ is far away from $\varepsilon_{\mathrm{G}}$, the unpaired nucleobases act as strong potential barriers or wells and the electrons will mainly propagate along relatively short pathways, i.e., the former three pathways. This gives rise to the splitting of an original transmission peak into a pair of minor peaks. When $E$ is shifted toward the energy gap, the scattering from the unpaired nucleobases will be gradually weakened, and the electron transport through the second and third pathways becomes more and more pronounced. As a result, the quantum interference among different pathways should be progressively enhanced, leading to the increment of the left (right) minor peak in the right (left) band and further separation of these two minor peaks (see the right band and the other energy region distant from the energy gap in the left band in Fig. 2). While in the weak scattering regime where $E$ locates in the vicinity of $\varepsilon_{\mathrm{G}}$ with $|E-\varepsilon_{\mathrm{G}}| < |t_{\mathrm{GG}}|$, the scattering from the unpaired nucleobases is weak and the electrons can propagate through more pathways, including the latter two longer pathways in Eq. (7). Consequently, an original transmission peak will be divided into more than two minor peaks and the charge transport along the DNA tetrahedron becomes complicated when $E$ is close to the on-site energy of the unpaired nucleobases. Notice that the transmission profiles could be affected by the molecule-electrode coupling [68–72]. Further inspection indicates that the aforementioned phenomena hold for a wide range of the coupling between the DNA tetrahedron and the real electrodes. Nevertheless, the number of the transmission peaks and the magnitude of the conductance depend on the molecule-electrode coupling, because of the quantum-interference effect at the molecule-electrode interface [69]. In particular, the splitting of the transmission peaks will disappear in the weak molecule-electrode coupling regime (data not shown), because the electron transport through longer pathways becomes negligible due to the cooperative effect of strong reflection at the molecule-electrode interface and significant scattering from the unpaired nucleobases.

Despite the similarity of the transmission spectra at different drain electrodes, the transmission profiles depend on the drain position, which is related to the asymmetric structure caused by the source position. One can see from Fig. 1 that the electrons can propagate from $e_0$ to $e_3$ mediated by the multiple transport pathways as well, such as $D_0 \rightarrow \mathrm{OM} \rightarrow D_3$. Notice that this shortest pathway differs from the one, $D_0 \rightarrow \mathrm{RO} \rightarrow D_1$, of electron flowing from $e_0$ to $e_1$, because the number of the unpaired nucleobases in these two pathways is different. This leads to different magnitude of the conductances at $e_1$ and $e_3$ (see the black-solid and blue-dotted lines in Fig. 2). By contrast, the former three pathways in Eq. (7) are equivalent to those of electron flowing from $e_0$ to $e_2$ and thus there is no observable difference between the conductances at $e_1$ and $e_2$ when $E$ is far away from $\varepsilon_{\mathrm{G}}$ (see the black-solid and red-dashed lines in Fig. 2). The relationship among these transmission spectra can also be understood by analyzing the symmetry of the tetrahedral DNA device. By inspecting Fig. 1, it is clear that in the presence of the source electrode, the mirror symmetry is broken with respect to the normal plane across either the RO edge or the RM one, whereas it is almost preserved with respect to the normal plane through the OM edge. Therefore, the curve of $G_3 - E$ is different from the ones of $G_1 - E$ and $G_2 - E$, and the latter two curves almost coincide with each other.

We then consider the influence of the contact position and the on-site energy disorder by exploring the electron

flowing through the drain electrode $e_1$, and focus on the left electronic band for clarity. Figure 3(a) shows $G_1$ versus $E$ for typical contact positions $P$, which could be achieved by moving the source electrode $e_0$ along the RO edge, in the absence of the on-site energy disorder. In this case, the former three pathways in Eq. (7) are changed into

$$\begin{aligned} &P \to \overline{\mathrm{RO}} \to D_1, \\ &P \to \overline{\mathrm{RO}} \to D_0 \to \mathrm{RM} \to D_2 \to \mathrm{RB} \to D_1, \\ &\text{and} \\ &P \to \overline{\mathrm{RO}} \to D_0 \to \mathrm{OM} \to D_3 \to \mathrm{OB} \to D_1, \end{aligned} \tag{8}$$

where $\overline{\mathrm{RO}}$ denotes a segment of the RO edge. It is clear that the shortest pathway, $P \to \overline{\mathrm{RO}} \to D_1$, does not contain any unpaired nucleobase and the resulting scattering vanishes when the electrons pass through this pathway. As a result, the conductance at $e_1$ for $P \neq 0$ could be considerably enhanced over almost the entire energy spectrum compared to the case of $P = 0$, as can be seen from all the solid and black-dashed lines in Fig. 3(a). In particular, although this shortest pathway becomes shorter when $e_0$ moves toward $e_1$, the transmission spectra are quite similar for different $P$ and the number of the transmission peaks is nearly independent of $P$ [Fig. 3(a)]. This phenomenon is a smoking gun of the multiple transport pathways regarding

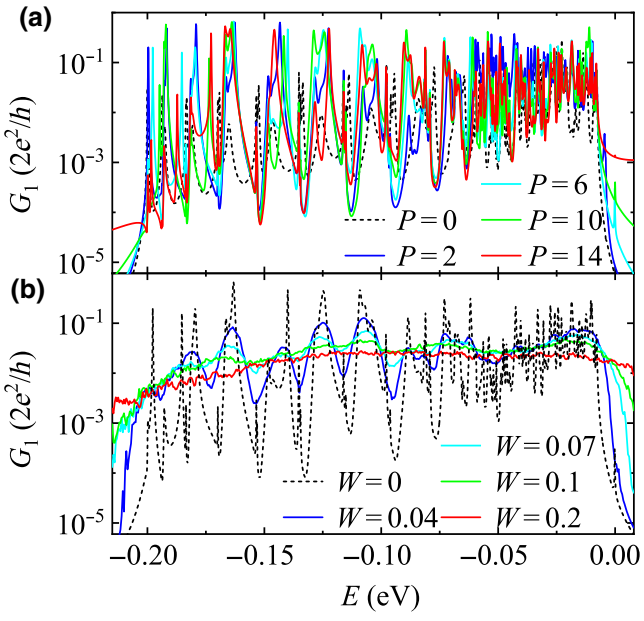


FIG. 3. Charge transport along the tetrahedral DNA device by considering the contact position and the on-site energy disorder. (a) $G_1$ versus $E$ for typical contact positions $P$ in the absence of the on-site energy disorder, $W = 0$. (b) $G_1$ versus $E$ for different disorder degrees $W$ with $P = 6$. Here, the black-dashed lines with $P = 0$ in (a) and $W = 0$ in (b) are shown for reference.

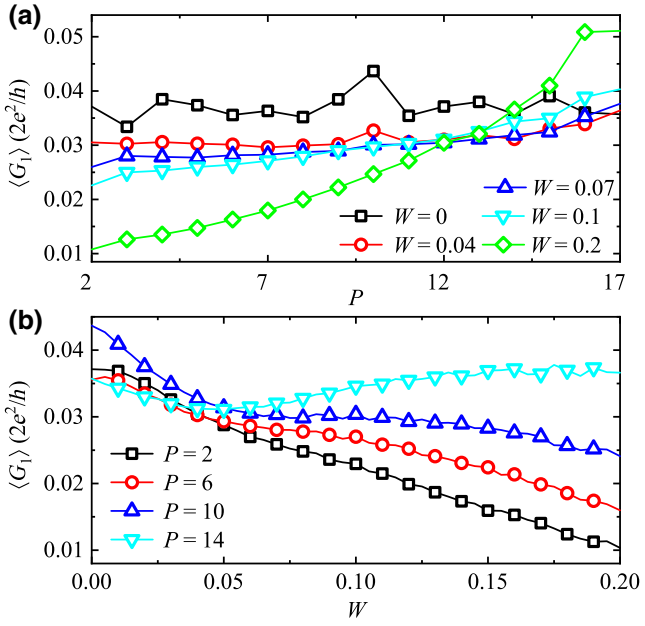


FIG. 4. Charge transport along the tetrahedral DNA device by considering the contact position and the on-site energy disorder. (a) Averaged conductance $\langle G_1 \rangle$ versus contact position $P$ for different disorder degrees $W$. (b) $\langle G_1 \rangle$ versus $W$ for typical values of $P$.

electron flowing from $e_0$ to $e_1$. Further inspection demonstrates that the averaged conductance $\langle G_1 \rangle$, obtained from the left band, is approximately independent of $P$ [see the black squares in Fig. 4(a)]. This is consistent with the electrochemical experiment of Ref. [51], in which the current flowing through the DNA tetrahedron is insensitive to the position of the redox molecule, since the current and the averaged conductance are equivalent to describe charge transport through the DNA tetrahedron. When $e_0$ deviates from the top vertex, the number of the unpaired nucleobases is different in the second and third pathways of Eq. (8), and correspondingly these two pathways are not equivalent. As a result, each original transmission peak will be split into more than two minor peaks [see the solid lines in Fig. 3(a)], and the charge transport along the DNA tetrahedron becomes more complicated in comparison to the case of $P = 0$.

Notice that the DNA tetrahedron can also be composed of inhomogeneous dsDNA molecules. And the electrochemical experiments are carried out in phosphate buffer solution [50–53], where counterions and water molecules may adsorb randomly around the DNA tetrahedron. These sequence inhomogeneity and environment effects could lead to on-site energy disorder, which usually brings forth detrimental effects for device applications. Here, we consider the most disordered case of Anderson disorder by adding a random variable $w_{jn}$ in the on-site energy $\varepsilon_{jn}$ [73], with $w_{jn}$ uniformly distributed within the range

$[-W/2, W/2]$ and $W$ the disorder degree. Figure 3(b) shows $G_1$ versus $E$ for typical disorder degrees $W$ with $P = 6$, which is calculated from an ensemble of 2000 disorder configurations. Once Anderson disorder is introduced, the electrons will experience stronger scattering when transmitting along longer pathways and preferentially propagate through the shortest pathway. As a result, the number of the transmission peaks is dramatically declined in the presence of Anderson disorder [see the black-dashed and blue-solid lines in Fig. 3(b)]. The larger the Anderson disorder is, the stronger scattering the electrons suffer. Consequently, both the magnitude and the oscillation amplitude of $G_1$ decrease with increasing $W$. In relatively weak disorder regime, however, $G_1$ can increase with $W$ around the transmission valleys [see the blue-solid, cyan-solid, and green-solid lines in Fig. 3(b)], because of the increment of the electronic states.

To further demonstrate the interplay between the contact position and the on-site energy disorder, the averaged conductance is calculated

$$\langle G_1 \rangle = \frac{1}{\Omega} \int_{\Omega} G_1 dE, \tag{9}$$

where $\Omega$ denotes the left electronic band. Figure 4(a) displays $\langle G_1 \rangle$ versus $P$ for several disorder degrees $W$. It is clear that the relationship between $\langle G_1 \rangle$ and $P$ strongly depends upon $W$. (i) In the absence of Anderson disorder, $\langle G_1 \rangle$ fluctuates around a certain value and is approximately independent of $P$ [see the black squares in Fig. 4(a)], because of the multiple transport pathways. (ii) In the weak disorder regime, when $e_0$ moves toward $e_1$, both the second and third pathways in Eq. (8) become longer and the scattering from these two pathways will be gradually enhanced. In the case that $e_0$ is distant from $e_1$, the electrons can propagate through the three pathways in Eq. (8) and then $\langle G_1 \rangle$ is insensitive to $P$ within the range $P \in [2, 14]$ [see the red circles and blue-up triangles in Fig. 4(a)], in accordance with the electrochemical experiment [51]. By contrast, when $e_0$ is close to $e_1$, the electron transport is mainly mediated by the shortest pathway. This pathway becomes shorter by shifting $e_0$ toward $e_1$ and the resulting scattering is gradually weakened, giving rise to almost linear increment of $\langle G_1 \rangle$ with $P$. (iii) In the strong disorder regime, the scattering from longer pathways is so strong that the electron transport through these pathways is negligible and is then mainly mediated by the shortest pathway. Similarly, when $e_0$ is shifted toward $e_1$, the shortest pathway becomes shorter and the resulting scattering progressively decays. This leads to monotonic increasing of $\langle G_1 \rangle$ with $P$ in the whole range $P \in [1, 16]$ [see the cyan-down triangles and green diamonds in Fig. 4(a)].

In addition, one can see from Fig. 4(a) that in the presence of Anderson disorder, different curves of $\langle G_1 \rangle - P$ intersect at about $P_c = 12$, where $\langle G_1 \rangle$ decreases with $W$ for $P < P_c$ and contrarily increases with $W$ for $P > P_c$. To further demonstrate this counterintuitive phenomenon of disorder-induced enhancement of the transmission ability, Fig. 4(b) plots $\langle G_1 \rangle$ versus $W$ for typical contact positions $P$. It clearly appears that the curves of $\langle G_1 \rangle - W$ are highly dependent on $P$. When $P = 2$, $\langle G_1 \rangle$ decreases almost linearly with increasing $W$ [see the black squares in Fig. 4(b)]. This is different from a single dsDNA molecule where the conductance decays exponentially with the disorder degree [74], which arises from the fact that the three pathways in Eq. (8) are approximately equivalent as $e_0$ is apart from the top vertex by only two nucleobases.

When $e_0$ is distant from the top vertex, however, the curves of $\langle G_1 \rangle - W$ are different for different $P$ and could be divided into three parts in general. (i) In the weak disorder regime, $\langle G_1 \rangle$ decreases quickly with $W$ as expected [see the beginning parts of the red circles, blue-up triangles, and cyan-down triangles in Fig. 4(b)], because the electron transport through all the pathways is declined owing to Anderson localization. (ii) When $W$ is increased and reaches the intermediate regime, although the scattering becomes stronger, $\langle G_1 \rangle$ decreases slowly with $W$ or is immune to $W$ [see the middle parts of the red circles and blue-up triangles in Fig. 4(b)]. In particular, $\langle G_1 \rangle$ can even increase with $W$ when $e_0$ is close to $e_1$ [see the middle part of the cyan-down triangles in Fig. 4(b)]. This disorder-induced enhancement of charge transport has been reported in other one- and two-dimensional systems [75,76], but the physical mechanism is different. Notice that with increasing $W$, the increasing rate of scattering from longer pathways is faster and consequently the electrons will preferentially propagate through the shortest pathway. In other words, the probability of electron transmission through the shortest pathway increases with $W$, which competes with the enhanced scattering from this pathway. When $e_0$ moves toward $e_1$, the probability of electron transmission through the shortest pathway is gradually enhanced, whereas the scattering from this pathway is declined. As a result, in the intermediate disorder regime, the electron flowing from $e_0$ to $e_1$ can be categorized into three mechanisms, ranging from disorder-induced suppression of charge transport to disorder-insensitive charge transport, and to disorder-enhanced charge transport, which strongly depend on $P$. (iii) In the strong disorder regime, the electron transmission through the shortest pathway is dramatically suppressed as well and thus $\langle G_1 \rangle$ decreases quickly with $W$ again, regardless of the contact position.

### B. Base-pair mismatch effect on charge transport along tetrahedral DNA devices

Next, we investigate the interplay between the contact position and a single base-pair mismatch in the RO edge. This base-pair mismatch is introduced by considering a

C-thymine (T) mismatch as in the electrochemical experiment [51], which occurs by replacing a G nucleobase with a T one. Correspondingly, the on-site energy is changed from $\varepsilon_{0M} = \varepsilon_G$ to $\varepsilon_{0M} = \varepsilon_T = 0.5$ eV [62–64], with $M$ the mismatched site. Previous experimental and theoretical works have shown that when a base-pair mismatch takes place, both $\pi$ stacking and hydrogen bonding, neighboring to the mismatched site, are dramatically declined, which arises from strong fluctuation of unstable mismatched base pair [28–36]. Then, both the intrastrand and interstrand couplings, linking to the T nucleobase, are reduced by one order of magnitude. As a result, the electrons could be considerably reflected by the C-T mismatched base pair.

Figure 5 presents the ratio $\langle G_1\rangle_{MM}/\langle G_1\rangle_{WM}$ as functions of contact position $P$ and mismatched site $M$. Here, $\langle G_1\rangle_{MM}$ denotes the averaged conductance in the presence of a single C-T mismatch and $\langle G_1\rangle_{WM}$ refers to the one without any base-pair mismatch, both of which are calculated from the left electronic band.

It clearly appears that the ratio $\langle G_1\rangle_{MM}/\langle G_1\rangle_{WM}$ depends strongly on the relative position of the source and the C-T base pair, and can be divided into three regions, i.e., $M > P$, $M = P$, and $M < P$. (i) For $M > P$ where the C-T base pair locates between $e_0$ and $e_1$, the electron transmission through the shortest pathway, $P \to \overline{\mathrm{RO}} \to D_1$, will be considerably declined due to strong scattering at the C-T base pair. As a result, the charge-transport ability at $e_1$ can be dramatically decreased by the C-T base pair and leads to a large green area with small ratio $\langle G_1\rangle_{MM}/\langle G_1\rangle_{WM} \in (0, 0.5)$, as can be seen from the upper left part in Fig. 5. This is consistent with the experiments that the charge-transport efficiency is considerably declined when the base-pair mismatch occurs between the redox molecule and the surface [51,53]. (ii) For $M < P$ where the C-T base pair situates between $e_0$ and $D_0$, the electron transmission through longer pathways, such as the second and third pathways in Eq. (8), will be decreased but less affected by the C-T base pair compared to the shortest pathway, because there are already other potential barriers of the unpaired nucleobases in longer pathways. Consequently, a yellow area with relatively large ratio $\langle G_1\rangle_{MM}/\langle G_1\rangle_{WM} \in (0.5, 1)$ is observed in the lower right part of Fig. 5. (iii) It is interesting that when the source is contacted at the mismatched site, $M = P$, the averaged conductance at $e_1$ could be enhanced by the C-T base pair with $\langle G_1\rangle_{MM}/\langle G_1\rangle_{WM} > 1$, which can be understood as follows. In this situation, the source is connected to the T and G nucleobases. Since the on-site energy of the T nucleobase is much higher than that of the G one, the electrons injected from the source will be dramatically reflected by the T nucleobase and thus the electron transmission through longer pathways is considerably blocked. As a result, the majority of the electrons will be injected into the G nucleobase and the electron transport is mainly mediated by the shortest pathway, which leads to the C-T mismatch-induced enhancement of charge transport observed at $e_1$.

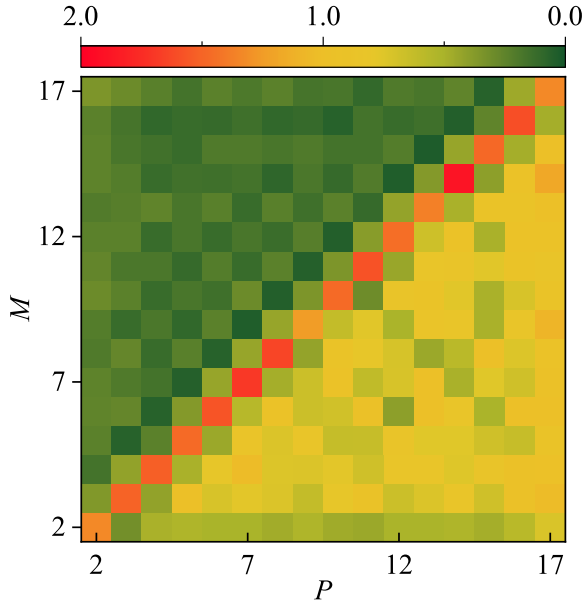


FIG. 5. Charge transport along the tetrahedral DNA device by taking into account the contact position and a single base-pair mismatch in the RO edge. A contour plot of the ratio $\langle G_1\rangle_{MM}/\langle G_1\rangle_{WM}$ as functions of contact position $P$ and base-pair mismatched site $M$. Here, $\langle G_1\rangle_{MM}$ corresponds to the averaged conductance in the presence of base-pair mismatch and $\langle G_1\rangle_{WM}$ to the one without any base-pair mismatch.

### C. Spin-filtering effect of tetrahedral DNA devices

Finally, we study the spin-polarized electron transport along the DNA tetrahedron, where the spin polarization at the $j$ th drain $e_j$ is defined as

$$P_{sj} = \frac{G_{j\uparrow} - G_{j\downarrow}}{G_{j\uparrow} + G_{j\downarrow}}. \tag{10}$$

Here, $G_{j\uparrow}$ and $G_{j\downarrow}$ are, respectively, the spin-up and spin-down components of the conductance $G_j$ at $e_j$, which satisfies $G_j = G_{j\uparrow} + G_{j\downarrow}$.

Figure 6 shows $P_{s1}$ at $e_1$ (black-solid line) and $P_{s2}$ at $e_2$ (red-solid line) in the absence of the on-site energy disorder and the base-pair mismatch, while the inset displays $P_{s3}$ at $e_3$, as a function of the electron energy $E$. Here, the source is connected to the top vertex with $P = 0$. One can see from Fig. 6 that the spin transport through the DNA tetrahedron presents several intriguing phenomena, which are different from dsDNA molecules [6,60] and DNA hairpins [77]. (i) The DNA tetrahedron exhibits pronounced spin-filtering effect, regardless of specific drain position. Although each double-stranded edge contains only 17 base pairs with $N = 17$, the spin polarization can reach 70.0% at $e_1$, 61.8% at $e_2$, and 47.0% at $e_3$, which is

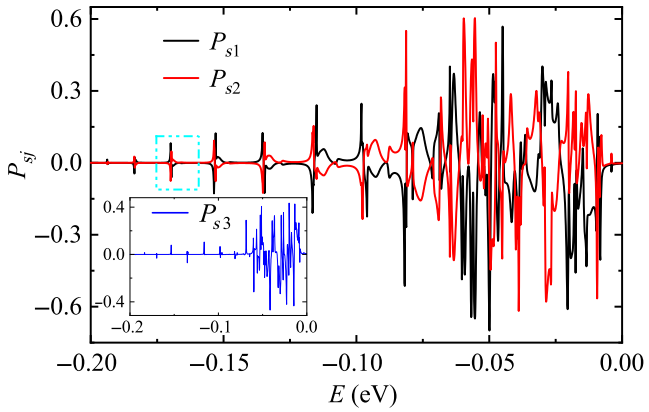


FIG. 6. Spin transport along the tetrahedral DNA device in the absence of the on-site energy disorder and the base-pair mismatch when the source electrode $e_0$ is contacted at the top vertex with $P = 0$. Energy-dependent spin polarization $P_{s1}$ at the drain electrode $e_1$ (black-solid line) and $P_{s2}$ at $e_2$ (red-solid line). The inset shows the spin polarization $P_{s3}$ at $e_3$.

comparable to long dsDNA molecules with length $N = 78$ [6,60]. This large spin polarization provides a smoking gun of longer transport pathways in the DNA tetrahedron, because the spin-filtering effect of chiral molecules can be enhanced with increasing the molecular length [6,60], further demonstrating the existence of the multiple pathways in the DNA tetrahedron. (ii) The spin polarization oscillates dramatically with increasing $E$, and the closer to the energy gap, the higher the oscillation frequency, which are independent of the drain position as well. When the spin polarization reaches the local maximum, the spin-polarized direction could be reversed by increasing $E$ slightly and the spin polarization quickly arrives at the local minimum (see the black-solid line in the cyan rectangle of Fig. 6), which is accompanied by the splitting of an original transmission peak into two minor peaks (see the left inset of Fig. 2). This stems from the quantum interference among different pathways and provides an alternative route to reverse the spin-polarized direction by slightly tuning the Fermi energy, instead of flipping the handedness of chiral molecules [60].

Despite the similarity of the spin-polarized profiles at different drain electrodes, the spin polarization considerably depends on the drain position. Although the curves of $G_1 - E$ and $G_2 - E$ are superimposed upon each other when $E$ is distant from the energy gap (see the black-solid and red-dashed lines in Fig. 2), the spin-polarized direction at $e_1$ is opposite to that at $e_2$ in almost the whole energy spectrum (see the black- and red-solid lines in Fig. 6). This may arise from the nearly preserved mirror symmetry with respect to the normal plane through the OM edge as discussed above. In this sense, the DNA tetrahedron could function as a nanoscale spin splitter, which separates spin-unpolarized electrons into spin-up electrons and spin-down ones. When spin-up electrons are detected at $e_1$, the spin-down ones could be observed at $e_2$, and vice versa.

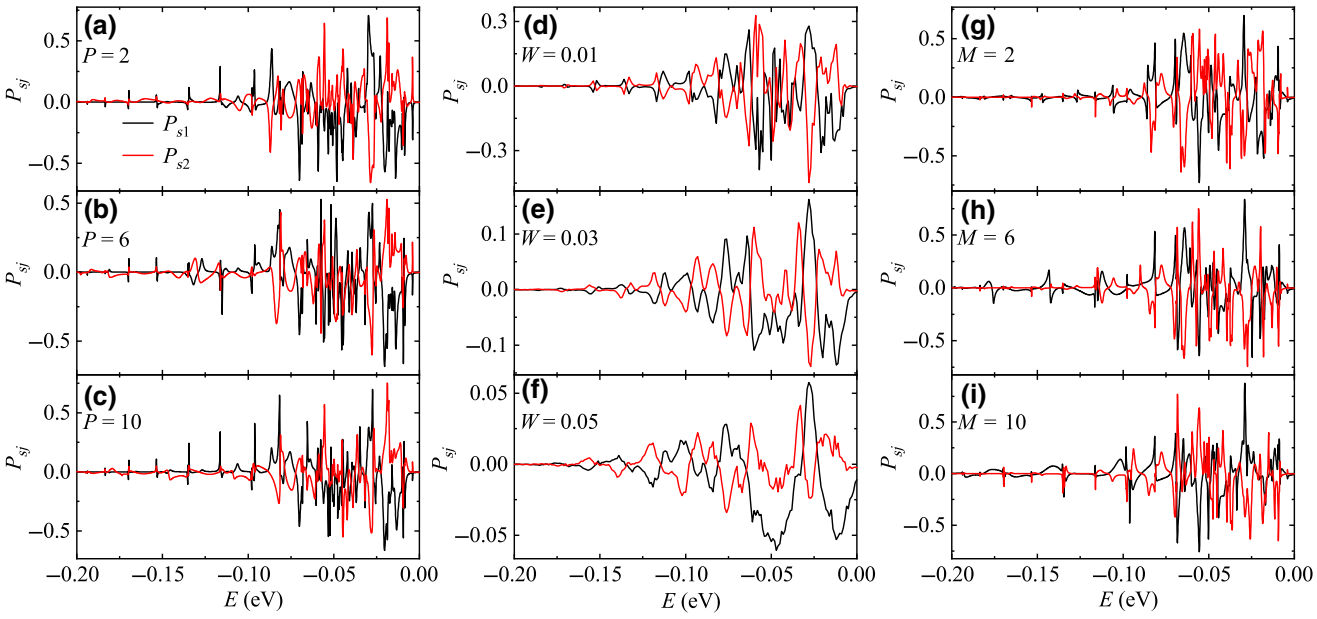


FIG. 7. Spin transport along the tetrahedral DNA device by taking into account the contact position, the on-site energy disorder, and the base-pair mismatch. (a)–(c) Energy-dependent $P_{s1}$ and $P_{s2}$ for typical contact positions $P$ in the absence of the on-site energy disorder and the base-pair mismatch. (d)–(f) Energy-dependent $P_{s1}$ and $P_{s2}$ for different disorder degrees $W$ with $P = 0$ and in the absence of the base-pair mismatch. (g)–(i) Energy-dependent $P_{s1}$ and $P_{s2}$ for different mismatched sites $M$ with $P = 0$ and $W = 0$. Here, all the black-solid lines correspond to $P_{s1}$ and all the red-solid ones to $P_{s2}$.

To further explore the spin-filtering effect of the DNA tetrahedron, we consider the influence of the contact position, the on-site energy disorder, and the base-pair mismatch, as illustrated in Figs. 7(a)–7(i), where all the black-solid lines refer to $P_{s1}$ and all the red-solid ones to $P_{s2}$. By inspecting Figs. 7(a)–7(c) and 7(g)–7(i), it clearly appears that although the profiles of the spin polarization may be distinct for different $P$ and $M$, the DNA tetrahedron exhibits significant spin-filtering effect, which is independent of the source position and the mismatched site. For example, $P_{s1}$ ($P_{s2}$) can achieve 70.7% (68.8%) for $P = 2$, 68.4% (60.1%) for $P = 6$, and 69.8% (75.1%) for $P = 10$, which are comparable to the case of $P = 0$ without any base-pair mismatch (Fig. 6). In addition, the curves of $P_{s1} - E$ and $P_{s2} - E$ for different $P$ [Figs. 7(a)–7(c)] and $M$ [Figs. 7(g)–7(i)] display dramatic oscillation with increasing $E$. In particular, the sign of $P_{s1}$ and $P_{s2}$ is opposite to each other over almost the whole energy spectrum, irrespective of the source position and the mismatched site as well. All of these phenomena are analogous to the case of $P = 0$ and $W = 0$ in the absence of base-pair mismatch. While in the presence of Anderson disorder, the spin-filtering effect will be gradually weakened by increasing $W$ [Figs. 7(d)–7(f)]. This can be traced back to the cooperative effect that the electron transport through longer pathways could be suppressed under Anderson disorder and the disorder induces additional detrimental effect for the spin selectivity. However, the spin-filtering effect remains significant in the weak disorder regime. For example, $P_{s1}$ ($P_{s2}$) can achieve 38.8% (44.8%) for $W = 0.01$, 16.2% (13.8%) for $W = 0.03$, and 6.1% (4.1%) for $W = 0.05$, which is accessible in experiments [14–16]. Furthermore, it is interesting that the phenomenon of the opposite sign between $P_{s1}$ and $P_{s2}$ still holds in the presence of Anderson disorder. Therefore, we conclude that the DNA tetrahedron could behave as a more efficient spin filter compared to dsDNA molecules and as a nanoscale spin splitter, which are robust against the contact position, the on-site energy disorder, and the base-pair mismatch. This theoretical prediction could be readily checked by, e.g., electrochemical experiments [50–53].

## IV. CONCLUSION

In summary, the charge transport in a multiterminal DNA tetrahedron has been studied by considering contact position, on-site energy disorder, and base-pair mismatch. The variation of the contact position is achieved by moving the source along one edge of the DNA tetrahedron, while keeping all of the three drains fixed at the bottom vertices. We find that this multiterminal DNA tetrahedron functions as a charge splitter when the source is contacted at the top vertex. And the charge-transport properties of the DNA tetrahedron strongly depend on the competition among the contact position, the on-site energy disorder, and the base-pair mismatch. (i) The dependence of charge-transport efficiency on the contact position relies on the on-site energy disorder. In the weak disorder regime, the charge-transport efficiency is approximately independent of the contact position. While in the strong disorder regime, the charge-transport efficiency increases monotonically by shifting the source toward the drain. The larger the disorder degree, the faster the increasing rate. (ii) The dependence of charge-transport efficiency on the on-site energy disorder is determined by the contact position. When the source is far from the drain, the charge-transport efficiency decreases almost linearly with the disorder degree. When the source is close to the drain, the charge-transport efficiency could be increased by increasing the disorder degree. (iii) The dependence of charge-transport efficiency on the base-pair mismatch is also determined by the contact position. When the base-pair mismatch occurs between the source and the drain, the charge-transport efficiency could be dramatically declined. When the base-pair mismatch occurs at the contact position, the charge-transport efficiency could be enhanced. (iv) Finally, we predict that the DNA tetrahedron could act as a more efficient spin filter compared to double-stranded DNA. In particular, opposite spin polarization could be observed at different drains. This may allow for designing a spin splitter, where spin-up electrons accumulate in one drain and spin-down electrons in another drain. Further studies may focus on charge transport through other DNA tetrahedra composed of inhomogeneous double-stranded DNA, because a single double-stranded DNA of different sequences exhibits a variety of phenomena, see, e.g., Refs. [78–81].

## ACKNOWLEDGMENTS

This work is supported by the National Natural Science Foundation of China (Grants No. 11874428, No. 11874187, and No. 11921005), the National Key Research and Development Program of China (Grant No. 2017YFA0303301), and the High Performance Computing Center of Central South University.

[1] D. D. Eley and D. I. Spivey, Semiconductivity of organic substances. Part 9.–Nucleic acid in the dry state, Trans. Faraday Soc. **58**, 411 (1962).
[2] R. G. Endres, D. L. Cox, and R. R. P. Singh, Colloquium: The quest for high-conductance DNA, Rev. Mod. Phys. **76**, 195 (2004).
[3] Charge Migration in DNA: Perspectives from Physics, Chemistry, and Biology, edited by T. Chakraborty (Springer, New York, 2007).
[4] J. C. Genereux and J. K. Barton, Mechanisms for DNA charge transport, Chem. Rev. **110**, 1642 (2010).

[5] F. Evers, R. Korytár, S. Tewari, and J. M. van Ruitenbeek, Advances and challenges in single-molecule electron transport, Rev. Mod. Phys. **92**, 035001 (2020).

[6] B. Göhler, V. Hamelbeck, T. Z. Markus, M. Kettner, G. F. Hanne, Z. Vager, R. Naaman, and H. Zacharias, Spin selectivity in electron transmission through self-assembled monolayers of double-stranded DNA, Science **331**, 894 (2011).

[7] C. Bruot, J. L. Palma, L. Xiang, V. Mujica, M. A. Ratner, and N. Tao, Piezoresistivity in single DNA molecules, Nat. Commun. **6**, 8032 (2015).

[8] L. Xiang, J. L. Palma, C. Bruot, V. Mujica, M. A. Ratner, and N. Tao, Intermediate tunnelling-hopping regime in DNA charge transport, Nat. Chem. **7**, 221 (2015).

[9] C. Guo, K. Wang, E. Zerah-Harush, J. Hamill, B. Wang, Y. Dubi, and B. Xu, Molecular rectifier composed of DNA with high rectification ratio enabled by intercalation, Nat. Chem. **8**, 484 (2016).

[10] Y. Li, L. Xiang, J. L. Palma, Y. Asai, and N. Tao, Thermoelectric effect and its dependence on molecular length and sequence in single DNA molecules, Nat. Commun. **7**, 11294 (2016).

[11] L. Xiang, J. L. Palma, Y. Li, V. Mujica, M. A. Ratner, and N. Tao, Gate-controlled conductance switching in DNA, Nat. Commun. **8**, 14471 (2017).

[12] R. Zhuravel, H. Huang, G. Polycarpou, S. Polydorides, P. Motamarri, L. Katrivas, D. Rotem, J. Sperling, L. A. Zotti, A. B. Kotlyar, J. C. Cuevas, V. Gavini, S. S. Skourtis, and D. Porath, Backbone charge transport in double-stranded DNA, Nat. Nanotechnol. **15**, 836 (2020).

[13] R. Naaman and D. H. Waldeck, Chiral-induced spin selectivity effect, J. Phys. Chem. Lett. **3**, 2178 (2012).

[14] R. Naaman, Y. Paltiel, and D. H. Waldeck, Chiral molecules and the electron spin, Nat. Rev. Chem. **3**, 250 (2019).

[15] S.-H. Yang, R. Naaman, Y. Paltiel, and S. S. P. Parkin, Chiral spintronics, Nat. Rev. Phys. **3**, 328 (2021).

[16] D. H. Waldeck, R. Naaman, and Y. Paltiel, The spin selectivity effect in chiral materials, APL Mater. **9**, 040902 (2021).

[17] O. B. Dor, S. Yochelis, S. P. Mathew, R. Naaman, and Y. Paltiel, A chiral-based magnetic memory device without a permanent magnet, Nat. Commun. **4**, 2256 (2013).

[18] K. Banerjee-Ghosh, O. B. Dor, F. Tassinari, E. Capua, S. Yochelis, A. Capua, S.-H. Yang, S. S. P. Parkin, S. Sarkar, L. Kronik, L. T. Baczewski, R. Naaman, and Y. Paltiel, Separation of enantiomers by their enantiospecific interaction with achiral magnetic substrates, Science **360**, 1331 (2018).

[19] A. V. Malyshev, DNA Double Helices for Single Molecule Electronics, Phys. Rev. Lett. **98**, 096801 (2007).

[20] S. S. Mallajosyula and S. K. Pati, Structure and Transport Characteristics of Modified DNA with Magnetic Ions, Phys. Rev. Lett. **98**, 136601 (2007).

[21] C.-T. Shih, S. Roche, and R. A. Römer, Point-Mutation Effects on Charge-Transport Properties of the Tumor-Suppressor Gene p53, Phys. Rev. Lett. **100**, 018105 (2008).

[22] B. Tan, M. Hodak, W. Lu, and J. Bernholc, Charge transport in DNA nanowires connected to carbon nanotubes, Phys. Rev. B **92**, 075429 (2015).

[23] A.-M. Guo and Q.-F. Sun, Topological states and quantized current in helical organic molecules, Phys. Rev. B **95**, 155411 (2017).

[24] H.-Z. Tang, Q.-F. Sun, J.-J. Liu, and Y.-T. Zhang, Majorana zero modes in regular B-form single-stranded DNA proximity-coupled to an s-wave superconductor, Phys. Rev. B **99**, 235427 (2019).

[25] A.-M. Guo, P.-J. Hu, X.-H. Gao, T.-F. Fang, and Q.-F. Sun, Topological phase transitions of thouless charge pumping realized in helical organic molecules with long-range hopping, Phys. Rev. B **102**, 155402 (2020).

[26] A. Aggarwal, A. K. Sahoo, S. Bag, V. Kaliginedi, M. Jain, and P. K. Maiti, Fine-tuning the DNA conductance by intercalation of drug molecules, Phys. Rev. E **103**, 032411 (2021).

[27] Q. Chen, A.-M. Guo, J. Liu, F. M. Peeters, and Q.-F. Sun, Topological phase transitions and majorana zero modes in DNA double helix coupled to s-wave superconductors, New J. Phys. **23**, 093047 (2021).

[28] S. O. Kelley, E. M. Boon, J. K. Barton, N. M. Jackson, and M. G. Hill, Single-base mismatch detection based on charge transduction through DNA, Nucleic Acids Res. **27**, 4830 (1999).

[29] B. Giese and S. Wessely, The influence of mismatches on long-distance charge transport through DNA, Angew. Chem. Int. Ed. **39**, 3490 (2000).

[30] P. K. Bhattacharya and J. K. Barton, Influence of intervening mismatches on long-range guanine oxidation in DNA duplexes, J. Am. Chem. Soc. **123**, 8649 (2001).

[31] F. Shao, M. A. O'Neill, and J. K. Barton, Long-range oxidative damage to cytosines in duplex DNA, Proc. Natl. Acad. Sci. USA **101**, 17914 (2004).

[32] J. Hihath, B. Xu, P. Zhang, and N. Tao, Study of single-nucleotide polymorphisms by means of electrical conductance measurements, Proc. Natl. Acad. Sci. USA **102**, 16979 (2005).

[33] Y. Osakada, K. Kawai, M. Fujitsuka, and T. Majima, Kinetics of charge transfer in DNA containing a mismatch, Nucleic Acids Res. **36**, 5562 (2008).

[34] N. Edirisinghe, V. Apalkov, J. Berashevich, and T. Chakraborty, Electrical current through DNA containing mismatched base pairs, Nanotechnology **21**, 245101 (2010).

[35] M. H. Lee, S. Avdoshenko, R. Gutierrez, and G. Cuniberti, Charge migration through DNA molecules in the presence of mismatches, Phys. Rev. B **82**, 155455 (2010).

[36] S. Mishra, V. S. Poonia, C. Fontanesi, R. Naaman, A. M. Fleming, and C. J. Burrows, Effect of oxidative damage on charge and spin transport in DNA, J. Am. Chem. Soc. **141**, 123 (2019).

[37] N. C. Seeman, DNA in a material world, Nature **421**, 427 (2003).

[38] H. Yan, T. H. LaBean, L. Feng, and J. H. Reif, Directed nucleation assembly of DNA tile complexes for barcode-patterned lattices, Proc. Natl. Acad. Sci. USA **100**, 8103 (2003).

[39] R. P. Goodman, R. M. Berry, and A. J. Turberfield, The single-step synthesis of a DNA tetrahedron, Chem. Commun., 1372 (2004).

[40] R. P. Goodman, I. A. T. Schaap, C. F. Tardin, C. M. Erben, R. M. Berry, C. F. Schmidt, and A. J. Turberfield, Rapid chiral assembly of rigid DNA building blocks for molecular nanofabrication, Science **310**, 1661 (2005).

[41] P. W. K. Rothemund, Folding DNA to create nanoscale shapes and patterns, Nature **440**, 297 (2006).
[42] S. M. Douglas, H. Dietz, T. Liedl, B. Högberg, F. Graf, and W. M. Shih, Self-assembly of DNA into nanoscale three-dimensional shapes, Nature **459**, 414 (2009).
[43] E. S. Andersen, M. Dong, M. M. Nielsen, K. Jahn, R. Subramani, W. Mamdouh, M. M. Golas, B. Sander, H. Stark, C. L. P. Oliveira, J. S. Pedersen, V. Birkedal, F. Besenbacher, K. V. Gothelf, and J. Kjems, Self-assembly of a nanoscale DNA box with a controllable lid, Nature **459**, 73 (2009).
[44] W. Zhu, A.-M. Guo, and Q.-F. Sun, Electronic transport through tetrahedron-structured DNA-like system, Front. Phys. **9**, 774 (2014).
[45] S. Li, T. Tian, T. Zhang, X. Cai, and Y. Lin, Advances in biological applications of self-assembled DNA tetrahedral nanostructures, Mater. Today **24**, 57 (2019).
[46] A. S. Walsh, H. Yin, C. M. Erben, M. J. A. Wood, and A. J. Turberfield, DNA cage delivery to mammalian cells, ACS Nano **5**, 5427 (2011).
[47] Z. Xia, P. Wang, X. Liu, T. Liu, Y. Yan, J. Yan, J. Zhong, G. Sun, and D. He, Tumor-penetrating peptide-modified DNA tetrahedron for targeting drug delivery, Biochemistry **55**, 1326 (2016).
[48] Q. Li, D. Zhao, X. Shao, S. Lin, X. Xie, M. Liu, W. Ma, S. Shi, and Y. Lin, Aptamer-modified tetrahedral DNA nanostructure for tumor-targeted drug delivery, ACS Appl. Mater. Interfaces **9**, 36695 (2017).
[49] H. Ding, J. Li, N. Chen, X. Hu, X. Yang, L. Guo, Q. Li, X. Zuo, L. Wang, Y. Ma, and C. Fan, DNA nanostructure-programmed like-charge attraction at the cell-membrane interface, ACS Cent. Sci. **4**, 1344 (2018).
[50] H. Pei, N. Lu, Y. Wen, S. Song, Y. Liu, H. Yan, and C. Fan, A DNA nanostructure-based biomolecular probe carrier platform for electrochemical biosensing, Adv. Mater. **22**, 4754 (2010).
[51] N. Lu, H. Pei, Z. Ge, C. R. Simmons, H. Yan, and C. Fan, Charge transport within a three-dimensional DNA nanostructure framework, J. Am. Chem. Soc. **134**, 13148 (2012).
[52] A. Abi, M. Lin, H. Pei, C. Fan, E. E. Ferapontova, and X. Zuo, Electrochemical switching with 3D DNA tetrahedral nanostructures self-assembled at gold electrodes, ACS Appl. Mater. Interfaces **6**, 8928 (2014).
[53] C. Li, X. Hu, J. Lu, X. Mao, Y. Xiang, Y. Shu, and G. Li, Design of DNA nanostructure-based interfacial probes for the electrochemical detection of nucleic acids directly in whole blood, Chem. Sci. **9**, 979 (2018).
[54] K. J. Cash, F. Ricci, and K. W. Plaxco, An electrochemical sensor for the detection of protein-small molecule interactions directly in serum and other complex matrices, J. Am. Chem. Soc. **131**, 6955 (2009).
[55] Y. Wen, H. Pei, Y. Wan, Y. Su, Q. Huang, S. Song, and C. Fan, DNA nanostructure-decorated surfaces for enhanced aptamer-target binding and electrochemical cocaine sensors, Anal. Chem. **83**, 7418 (2011).
[56] Z. Ge, M. Lin, P. Wang, H. Pei, J. Yan, J. Shi, Q. Huang, D. He, C. Fan, and X. Zuo, Hybridization chain reaction amplification of microRNA detection with a tetrahedral DNA nanostructure-based electrochemical biosensor, Anal. Chem. **86**, 2124 (2014).
[57] M. Lin, P. Song, G. Zhou, X. Zuo, A. Aldalbahi, X. Lou, J. Shi, and C. Fan, Electrochemical detection of nucleic acids, proteins, small molecules and cells using a DNA-nanostructure-based universal biosensing platform, Nat. Protoc. **11**, 1244 (2016).
[58] P. Song, M. Li, J. Shen, H. Pei, J. Chao, S. Su, A. Aldalbahi, L. Wang, J. Shi, S. Song, L. Wang, C. Fan, and X. Zuo, Dynamic modulation of DNA hybridization using allosteric DNA tetrahedral nanostructures, Anal. Chem. **88**, 8043 (2016).
[59] P. Song, J. Shen, D. Ye, B. Dong, F. Wang, H. Pei, J. Wang, J. Shi, L. Wang, W. Xue, Y. Huang, G. Huang, X. Zuo, and C. Fan, Programming bulk enzyme heterojunctions for biosensor development with tetrahedral DNA framework, Nat. Commun. **11**, 838 (2020).
[60] A.-M. Guo and Q.-F. Sun, Spin-Selective Transport of Electrons in DNA Double Helix, Phys. Rev. Lett. **108**, 218102 (2012).
[61] Electronic Transport in Mesoscopic Systems, edited by S. Datta (Cambridge University Press, Cambridge, England, 1995).
[62] H. Zhang, X.-Q. Li, P. Han, X. Y. Yu, and Y. Yan, A partially incoherent rate theory of long-range charge transfer in deoxyribose nucleic acid, J. Chem. Phys. **117**, 4578 (2002).
[63] K. Senthilkumar, F. C. Grozema, C. F. Guerra, F. M. Bickelhaupt, F. D. Lewis, Y. A. Berlin, M. A. Ratner, and L. D. A. Siebbeles, Absolute rates of hole transfer in DNA, J. Am. Chem. Soc. **127**, 14894 (2005).
[64] L. G. D. Hawke, G. Kalosakas, and C. Simserides, Electronic parameters for charge transfer along DNA, Eur. Phys. J. E **32**, 291 (2010).
[65] A. Capobianco, A. Landi, and A. Peluso, Modeling DNA oxidation in water, Phys. Chem. Chem. Phys. **19**, 13571 (2017).
[66] A. Aggarwal, V. Vinayak, S. Bag, C. Bhattacharyya, U. V. Waghmare, and P. K. Maiti, Predicting the DNA conductance using a deep feedforward neural network model, J. Chem. Inf. Model. **61**, 106 (2021).
[67] S. Roche, Sequence Dependent DNA-Mediated Conduction, Phys. Rev. Lett. **91**, 108101 (2003).
[68] E. Maciá, F. Triozon, and S. Roche, Contact-dependent effects and tunneling currents in DNA molecules, Phys. Rev. B **71**, 113106 (2005).
[69] A.-M. Guo and S.-J. Xiong, Effects of contact and efficient charge transport in G4-DNA molecules, Phys. Rev. B **80**, 035115 (2009).
[70] Y. S. Joe, S. H. Lee, and E. R. Hedin, Electron transport through asymmetric DNA molecules, Phys. Lett. A **374**, 2367 (2010).
[71] S. Malakooti, E. R. Hedin, Y. D. Kim, and Y. S. Joe, Enhancement of charge transport in DNA molecules induced by the next nearest-neighbor effects, J. Appl. Phys. **112**, 094703 (2012).
[72] K. Lambropoulos and C. Simserides, Spectral and transmission properties of periodic 1D tight-binding lattices with a generic unit cell: An analysis within the transfer matrix approach, J. Phys. Commun. **2**, 035013 (2018).
[73] Y. Zhu, C.-C. Kaun, and H. Guo, Contact, charging, and disorder effects on charge transport through a model DNA molecule, Phys. Rev. B **69**, 245112 (2004).

[74] A.-M. Guo and Q.-F. Sun, Sequence-dependent spin-selective tunneling along double-stranded DNA, Phys. Rev. B **86**, 115441 (2012).

[75] L. Chen, F. Ouyang, S. Ma, T.-F. Fang, A.-M. Guo, and Q.-F. Sun, Enhancement of electron transport and band gap opening in graphene induced by adsorbates, Phys. Rev. B **101**, 115417 (2020).

[76] E. Zerah-Harush and Y. Dubi, Effects of disorder and interactions in environment assisted quantum transport, Phys. Rev. Res. **2**, 023294 (2020).

[77] P.-J. Hu, S.-X. Wang, X.-H. Gao, Y.-Y. Zhang, T.-F. Fang, A.-M. Guo, and Q.-F. Sun, Spin-dependent electron transport along hairpinlike DNA molecules, Phys. Rev. B **102**, 195406 (2020).

[78] A.-M. Guo, Long-range correlation and charge transfer efficiency in substitutional sequences of DNA molecules, Phys. Rev. E **75**, 061915 (2007).

[79] E. L. Albuquerque, U. L. Fulco, V. N. Freire, E. W. S. Caetano, M. L. Lyra, and F. A. B. F. de Moura, DNA-based nanobiostructured devices: The role of quasiperiodicity and correlation effects, Phys. Rep. **535**, 139 (2014).

[80] K. Lambropoulos and C. Simserides, Periodic, quasiperiodic, fractal, kolakoski, and random binary polymers: Energy structure and carrier transport, Phys. Rev. E **99**, 032415 (2019).

[81] K. Lambropoulos and C. Simserides, Tight-binding modeling of nucleic acid sequences: Interplay between various types of order or disorder and charge transport, Symmetry **11**, 968 (2019).